

Contents lists available at ScienceDirect

Journal of Crystal Growth

journal homepage: www.elsevier.com/locate/jcrysgro





Transition metal (dis)order in single crystal multicomponent rare earth perovskites

Lucas A. Pressley ^{a,b,*}, Hector K. Vivanco ^{a,b}, Tanya Berry ^{a,b}, Maxime A. Siegler ^a, Tyrel M. McQueen ^{a,b,c,**}

- ^a Department of Chemistry, The Johns Hopkins University, Baltimore, 21218, MD, USA
- b Institute for Quantum Matter, The William H. Miller III Department of Physics and Astronomy, The Johns Hopkins University, Baltimore, 21218, MD, USA
- ^c Department of Materials Science and Engineering, The Johns Hopkins University, Baltimore, 21218, MD, USA

ARTICLE INFO

Communicated by T. Duffar

Dataset link: https://data.paradim.org/, https://materialsautomated.github.io/

Keywords:

A2. Floating zone

- B1.High entropy oxides
- B2. Magnetic materials
- B1. Perovskite
- A2. Laser diode floating zone
- B2. Spin glass

ABSTRACT

The utilization of configurational entropy in materials design has accelerated the tailoring of oxides for a variety of technological applications. So called "high entropy" oxides (HEO) have more recently been investigated for their use in magnetocaloric refrigeration due to tunability of the spin glass phase. To advance our understanding of these magnetic interactions, we have grown single crystals (5 mm diameter, 3 cm length) of the multicomponent perovskite $SmCo_{1/4}Cr_{1/4}Fe_{1/4}Mn_{1/4}O_3$ using the laser diode floating zone technique. This material deviates from its parent $SmMO_3$ (M=Co, Cr, Fe, Mn) magnetic behaviors by having two broad transitions with a large bifurcation in the zero-field cooled vs field cooled measurements. Measurements of magnetization as a function of field show spin canting of the transition metal ions, with exchange bias emerging as a function of temperature. Heat capacity measurements are utilized alongside the non-magnetic rare earth analog $LaCo_{1/4}Cr_{1/4}Fe_{1/4}Mn_{1/4}O_3$ to understand the low temperature superexchange interactions. Such comparison supports the two magnetic sublattices operating at different energy scales. Overall single crystal growth of such HEO should be utilized due to the ease of growth using the floating zone technique and insight it gives into the magnetic characterization.

1. Introduction

High entropy materials, multicomponent systems with a high configurational entropy term, i.e., a large positive ΔS due to compositional disorder, have received an explosion of interest in the recent years due to the impact the disorder can have on the properties, an example seen in Ni super-alloys and coatings to protect from corrosion [1-3]. In the area of high entropy oxides (HEO), in particular systems with multiple components on the cation sublattice, there are intriguing questions regarding the presence of the local order/disorder in accordance with the single-phase structure present in these ceramics [4-6]. This naturally impacts the magnetic exchange interactions and gives rise to the question of whether there is complete disorder or does new behavior emerge distinct from the parents' ala a "cocktail effect" [7,8]. The perovskite structure serves as an attractive target thanks to its flexibility to accommodate a wide range of cations in the lattice [9]. Bulk single crystals are essential in these studies to allow for more characterization tools in both crystal structure and magnetism. Currently bulk single

crystal growth for high entropy/multicomponent materials has only been briefly explored [10-14].

We report the first synthesis of bulk single crystals of HEO perovskite $SmCo_{1/4}Cr_{1/4}Fe_{1/4}Mn_{1/4}O_3$ using a laser diode floating zone furnace. Single crystal X-ray diffraction data (SCXRD) shows the material crystallizes in a distorted orthorhombic perovskite structure in the space group Pnma. DC magnetization measurements show antiferromagnetic ordering with spin glassiness suggested according to differences in zero-field and field cooled measurements. Magnetization as a function of field shows temperature dependent hysteresis indicative of spin canting of the transition metals with ferrimagnetic interactions. Compared to the parent $SmMO_3$ (M = Co, Cr, Fe, Mn) perovskites, these transitions occur at different temperatures, with the HEO lacking the complete reversal in magnetization seen in $SmFeO_3$ due to the ferrimagnetic behavior between the disordered transition metals [15]. The non-magnetic rare earth analog of $LaCo_{1/4}Cr_{1/4}Fe_{1/4}Mn_{1/4}O_3$ shows that Sm interaction with the transition metal sublattice increases as

E-mail addresses: lpj@ornl.gov (L.A. Pressley), mcqueen@jhu.edu (T.M. McQueen).

^{*} Corresponding author at: Department of Chemistry, The Johns Hopkins University, Baltimore, 21218, MD, USA.

^{**} Corresponding author.

temperature decreases, with heat capacity measurements used to extract out the Sm magnetic contribution from the phonon behavior. Overall, this paper supports the use of the floating zone technique in synthesizing bulk single crystals of high entropy materials of interest and shows the impact disorder can have even for a "low entropy" HEO.

2. Materials and methods

Starting rare earth oxides La $_2$ O $_3$ (Alfa Aesar 99.99% E12W028) and Sm $_2$ O $_3$ (Alfa Aesar 99.99%, T24B047) were dried at T $\sim 1000~^{\circ}$ C overnight. Rare earth oxides were weighed out along with Co $_3$ O $_4$ (NOAH Technologies 99.5% 100541), CrO $_2$ (Dupont), Fe $_3$ O $_4$ (Cerac 99.5%, X8089), and MnO $_2$ (NOAH Technologies 99.9% 211512) targeting the formula LnCo $_1/4$ Cr $_1/4$ Fe $_1/4$ Mn $_1/4$ O $_3$ and mixed intimately in an agate mortar and pestle. SmCo $_1/4$ Cr $_1/4$ Fe $_1/4$ Mn $_1/4$ O $_3$ were heated as loose powder in an uncovered alumina boat in a horizontal tube furnace at T $\sim 1450~^{\circ}$ C for 12 h with a ramp rate of 100 $^{\circ}$ C/h and allowed to cool to room temperature over 12 h. LaCo $_1/4$ Cr $_1/4$ Fe $_1/4$ Mn $_1/4$ O $_3$ powder was prepared similarly, but with a dwell temperature of T $\sim 1350~^{\circ}$ C instead of T $\sim 1450~^{\circ}$ C.

SmCo_{1/4}Cr_{1/4}Fe_{1/4}Mn_{1/4}O₃ were compacted into rod shapes using rubber balloons, evacuated, and subsequently subjected to hydro-static pressure (~75 MPa). Upon removal from the balloon, the rods were sintered in an open alumina boat in a box furnace at T~ 1450 °C for 12 h with a ramp rate of 100 °C/h and allowed to cool to room temperature over 12 h. The sintered rods were mounted in a Laser Diode Floating Zone (LDFZ) furnace (Crystal Systems, Inc., FD-FZ-5-200-VPO-PC) with 5×200 W GaAs lasers ($\lambda = 976$ nm); the seed rod was affixed to an alumina holder on the lower shaft using Nichrome wire while the feed rod was suspended from a hook on the upper shaft using Nichrome wire. An applied pressure of 2 bar of $O_{2(g)}$ was used flowing at 250 mL/min with lasers tilted at 5° above the plane. The seed rod was melted, and the feed rod was joined to create a stable molten zone. Both rods were translated downward through the hot zone. The steady state conditions were found to occur when the upper and lower shaft traveled at a rate of 5.5 and 5 mm/h respectively while counter rotating at 10 rpm.

Heat capacity measurements from T = 2–300 K were taken with a Quantum Design Physical Properties Measurement System (PPMS) using the semi adiabatic pulse method with a 1% temperature rise. Phonon subtraction of heat capacity using the La containing analog was performed by scaling according to Hofmann and extrapolating to T=0 K [16,17]. Magnetization data were collected as a function of temperature and field from T = 2–300 K and $\mu_0H=-7$ to 7 T on both powder and aligned crystals using a Quantum Design Magnetic Property Measurement System (MPMS). Energy dispersive X-ray spectroscopy (EDS) to estimate transition metal ratios was performed using a JEOL JSM IT100 scanning electron microscope (SEM) at 20 keV operating in backscatter mode.

Laboratory-based X-ray diffraction patterns of the powder and ground up single crystals were collected using a Bruker D8 Focus diffractometer with Cu K_{α} radiation and a LynxEye position sensitive detector. Rietveld refinements to check phase purity were performed using Bruker TOPAS software (Version 4.2, Bruker AXS). For the SCXRD analysis, all reflection intensities were measured at 213(2) K using a Rigaku Oxford Diffraction SuperNova diffractometer (equipped with Atlas detector) with Mo K_{α} radiation ($\lambda = 0.71073$ Å) under the program CrysAlisPro (Version CrysAlisPro 1.171.42.49, Rigaku OD, 2022). The same program was used to refine the cell dimensions and for data reduction. The structure was solved with the program SHELXS-2018/3 and was refined on F^2 with SHELXL-2018/3 [18]. Data were corrected for absorption using an analytical numeric absorption correction using a multifaceted crystal model under CrysAlisPro. The temperature of the data collection was controlled using the system Cryojet (manufactured by Oxford Instruments). The occupancy of the 3d transition metals were fixed at 0.25 according to input stoichiometries and absence of impurity phase in PXRD. Crystal structure were visualized using VESTA [19]. Magnetic entropy change was determined from interpolated magnetization data using code derived from Bocarsly et al. [20] Point charge calculations for Sm³⁺ were performed using PyCrystalField [21].

3. Results and discussion

3.1. High entropy classification

In the discussion of HEO, there is a distinction of entropy stabilized vs high entropy that should be noted [22,23]. The family of HEO LnMO₃ are shown to be phase pure when cooled slowly, so the configurational entropy is not decisive to the stability of the phase, compared to other systems such as the HEO rock salt $\mathrm{Co_{0.2}Cu_{0.2}Mg_{0.2}Ni_{0.2}Zn_{0.2}O}$ [24,25]. Commonly in designing HE materials, a 5-component equimolar substitution is instituted on the sublattice and has been done for previously synthesized HEO perovskites [26]. Initial attempts to synthesize the 5-component $Sm(Co_{0,2}Cr_{0,2}Fe_{0,2}Mn_{0,2}Ni_{0,2})O_3$ were successful for powder form but crystal growth using the floating zone method resulted in an impurity of NiO in PXRD of the grown crystal. This is due to Ni3+ requiring high oxidizing conditions for crystal growth, as seen in the rare earth nickelates [27,28]. Given the multiple valence states optional for many of these transition metals, it is likely that each element is in the 3+ state based on this experiment, further supported by the calculated bond valence sums approximating 3 [29].

Much discussion has been had concerning label of "high entropy" for materials and its impact [30,31]. For this material for example, the configurational entropy per formula unit is 1.39R, where is the R molar gas constant. This traditionally places it in the category of medium entropy. If one accounts for the other sublattices and calculate this per atom, the categorization drops to 0.28R, firmly in low entropy. If one uses an entropy metric to account for different sublattices, the calculated value is 0.84, keeping it under the classification of low entropy [32]. In the case of HEO $LnMO_3$, we see that the configurational entropy likely is not the leading contribution to its behavior but instead the chemically complex exchange interactions occurring. Due to familiarity, we will keep the using the term HEO to emphasize the design concept rather than the inherent classification.

3.2. Crystal structure and composition

Single crystal structure solution of HEO SmMO₃ shows the material crystallizes in space group Pnma with the structure type GdFeO3, with the resulting parameters shown in Table 1 [33]. This is a distorted orthorhombic perovskite as visualized in Fig. 1a with Glazer notation $a^+b^-b^-$ [34]. The as-grown crystal is visualized in Fig. 1b. Due to the high fluorescence of the transition metals, analysis of the crystallinity by use of Laue diffraction was not feasible. Precession images were digitally reconstructed from raw SCXRD data and show no sign of twinning or streaking as shown in Fig. 1c along the (0kl) plane. Powder samples of both HEO SmMO3 and LaMO3 as well as the ground up crystal are seen as phase pure (both impurity free and a single perovskite phase) in PXRD. Due to the multicomponent substitution, occupancy was checked using EDS, results shown in Table 2, although the real error bars are likely larger due to the closeness in peak location. Mapping of the powder in Fig. 2 shows homogeneous distribution, evidence of a single-phase perovskite. Measurement of sample mass before and after firing showed a loss of 0.3%, discouraging the likelihood of offstoichoimetry by means of volatilization of starting materials. There was presence of vapor condensed on the quartz tube used for the LDFZ post crystal growth. PXRD of the vapor (Figure S1) can be indexed to CoCr₂O₄, which could account for the slight deficiency of Cr in the EDS measurements.

 $\label{eq:table 1} \textbf{Table 1} \\ \textbf{Crystallographic parameters of the SXRD for floating zone grown } \\ \textbf{SmCo}_{1/4} \\ \textbf{Cr}_{1/4} \\ \textbf{Fe}_{1/4} \\ \textbf{Mn}_{1/4} \\ \textbf{O}_3. \\ \textbf{O}_3. \\ \textbf{O}_{3/4} \\ \textbf{Cr}_{1/4} \\ \textbf{Fe}_{1/4} \\ \textbf{Mn}_{1/4} \\ \textbf{O}_3. \\ \textbf{O}_{3/4} \\ \textbf{Cr}_{1/4} \\ \textbf{Fe}_{1/4} \\ \textbf{Mn}_{1/4} \\ \textbf{O}_{3/4} \\ \textbf{O}_{3/4} \\ \textbf{Cr}_{1/4} \\ \textbf{Fe}_{1/4} \\ \textbf{Mn}_{1/4} \\ \textbf{O}_{3/4} \\$

Formula				$SmCo_{1/4}Cr_{1/4}Fe_{1/4}Mn_{1/4}O_3$													
Crystal system Space group a (Å) b (Å) c (Å) c (Å) c (Å) c (Å) c (A) c (A) c (A) c (A) c (A) c (A) c (B) c				Orthorhombic													
				Pnma (no. 99)													
				5.5568(2)													
				7.6367(3) 5.3679(2) 227.790(15) 1 Mo K_a , $\lambda = 0.71073 \text{ Å}$													
								213 31.21 446									
											Reflections collected/unique/internal data agreement Data/parameters				$6196/459, R_{int} = 0.048$ $459/29$		
								Goodness-of-fit $R = \sum_{j} F_o - F_c / \sum_{j} F_o $ $wR(F^2) = [\sum_{j} w(F_o^2 - F_c^2)^2 / \sum_{j} w(F_o^2)^2]^{1/2}$				1.18 0.017 0.040					
				Largest dif. peal	k/hole										1.660/-1.921	e Å-3	
					Occ.	Wyckoff positions	x (Å)								y (Å)	z (Å)	
				Co	1/4	4a	0.5	0	0.5								
Cr	1/4	4a	0.5	0	0.5												

	Occ.	Wyckoff positions	x (Å)	y (Å)	z (Å)	$U_{iso} (A^2)$
Co	1/4	4a	0.5	0	0.5	0.00380(14)
Cr	1/4	4a	0.5	0	0.5	0.00380(14)
Fe	1/4	4a	0.5	0	0.5	0.00380(14)
Mn	1/4	4a	0.5	0	0.5	0.00380(14)
Sm	1	4c	0.94341(4)	0.25	0.48773(4)	0.00560(10)
01	1	4c	0.4746(6)	-0.25	0.4096(7)	0.0081(6)
O2	1	8d	0.7018(4)	0.0470(3)	0.2008(4)	0.0084(4)
	$U_{11} (Å^2)$	U_{22} (Å ²)	$U_{33} (Å^2)$	$U_{12} (Å^2)$	$U_{13} (\mathring{A}^2)$	$U_{23} (Å^2)$
Co=Cr=Fe=Mn	0.0039(3)	0.0040(3)	0.0036(3)	-0.0003(2)	0.00007(19)	-0.00008(19)
Sm	0.00531(14)	0.00585(14)	0.00565(15)	0	0.00077(7)	0
01	0.0086(15)	0.0095(14)	0.0062(15)	0	0.0019(12)	0
02	0.0100(11)	0.0086(9)	0.0065(10)	0.0019(8)	-0.0015(9)	0.0014(8)

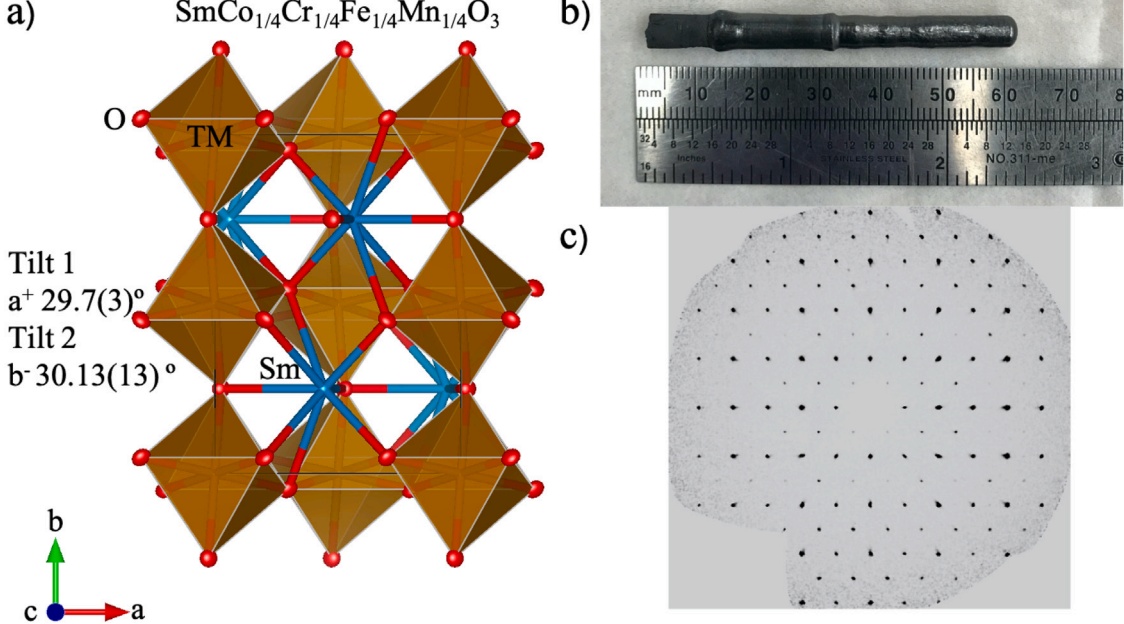


Fig. 1. (a) Crystal structure of $SmCo_{1/4}Cr_{1/4}Fe_{1/4}Mn_{1/4}O_3$ with Glazer notation $a^+b^-b^-$ for the tilted transition metal octahedra. Atomic displacement parameters are visualized at 80% probability (b) Floating zone grown crystal of $SmCo_{1/4}Cr_{1/4}Fe_{1/4}Mn_{1/4}O_3$ (c) Digitally reconstructed precession photograph from SCXRD data along the (0kl) plane.

 $\label{eq:table 2} \textbf{Elemental ratios for single crystal } SmCo_{1/4}Cr_{1/4}Fe_{1/4}Mn_{1/4}O_3 \ \ \text{as determined by EDS}.$

Element	Atom %
Co	6.09(21)
Cr	3.92(17)
Fe	4.70(23)
Mn	6.32(22)

3.3. Magnetization

Magnetization as a function of temperature in Fig. 3 shows a bifurcation occurring between the field cooled (FC) and zero field cooled (ZFC) at T~150 K for powder samples of SmMO $_3$. Two transitions, independent of cooling method, are seen to occur below room temperature, one around the bifurcation, the second being a broad hump with its maxima centered around T~12.5 K. Application of increasing field (up to $\mu_0H=7$ T) is shown in Fig. 3b to suppress this second

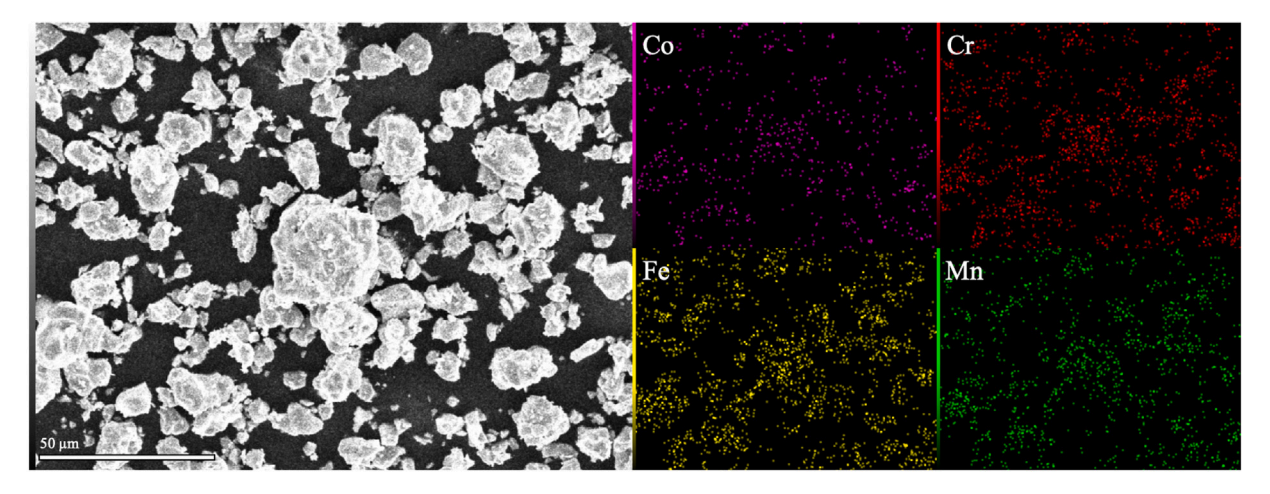
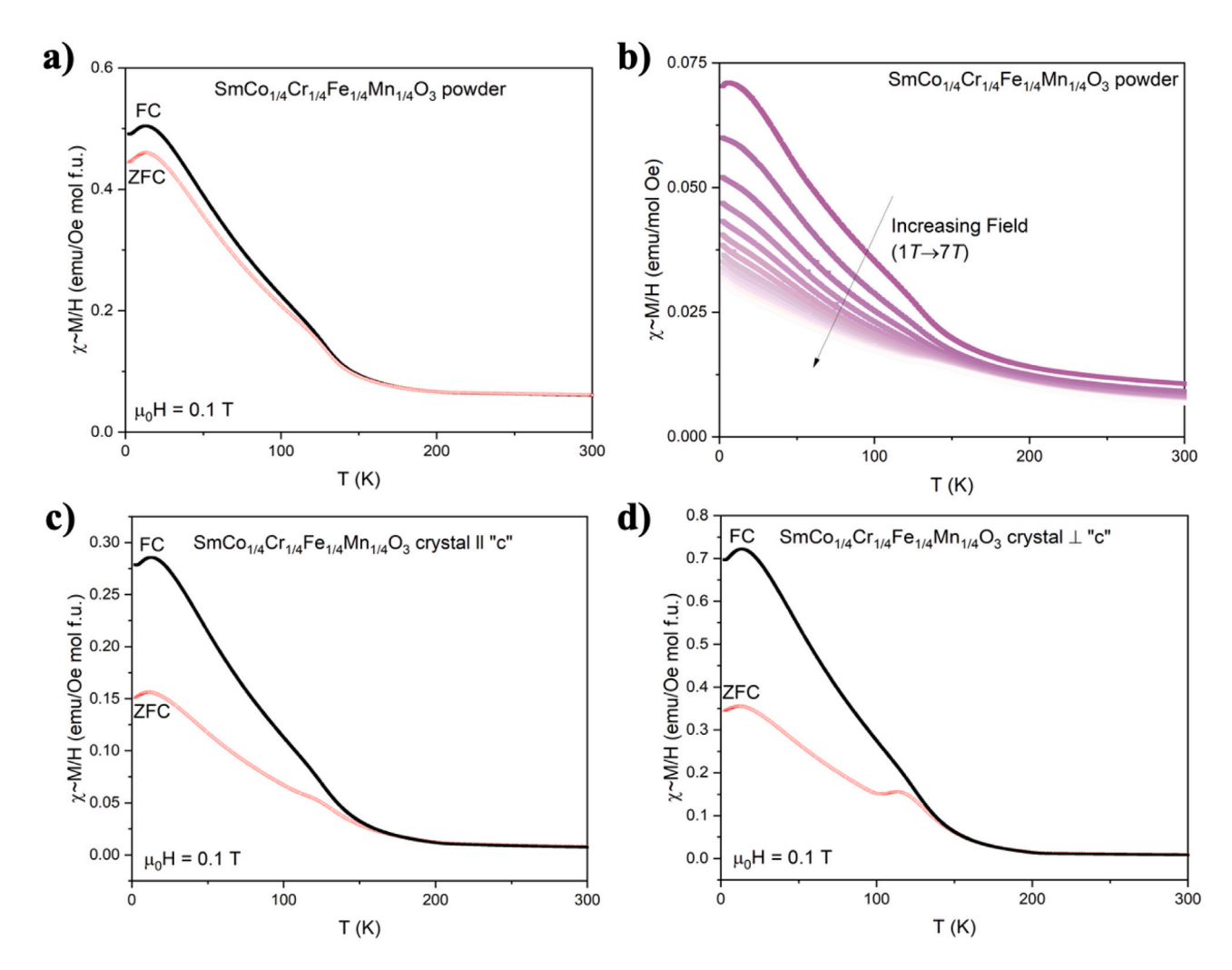


Fig. 2. SEM image of $SmCo_{1/4}Cr_{1/4}Fe_{1/4}Mn_{1/4}O_3$ powder with EDS mapping of the transition metal elements colored. (For interpretation of the references to color in this figure legend, the reader is referred to the web version of this article.)



transition. Measurements with field both parallel and perpendicular to single crystal in Fig. 3c and d show presence of anisotropy, indicated by differences in magnetic susceptibility, with divergence occurring around $T\sim200$ K. These values both differ from those of the powder, as expected given a distribution of crystalline axes in the latter. Both

magnetic transitions are still visible, with the perpendicular transitions now manifesting as broad humps under ZFC. Further, the bifurcation of ZFC and FC occurs at higher temperatures for both directions compared to the powder. A comparison with the non-magnetic rare earth analog $LaMO_3$ shows similar behavior at high temperatures among ZFC and

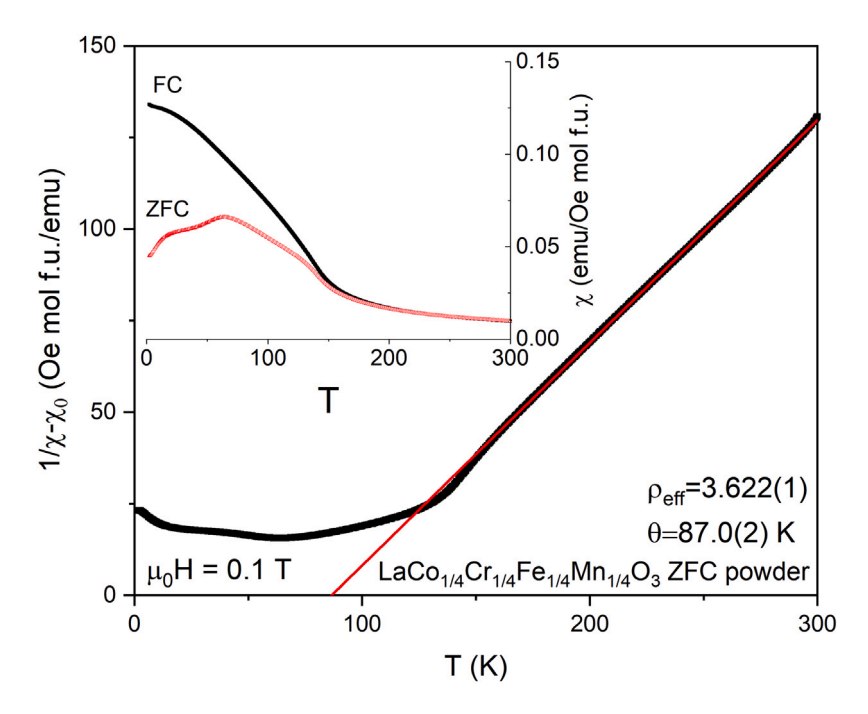


Fig. 4. Curie Weiss fit to the paramagnetic region of zero field cooled (ZFC) $LaCo_{1/4}Cr_{1/4}Fe_{1/4}Mn_{1/4}O_3$ powder. Inset shows the field cooled (FC) and zero field cooled (ZFC) magnetization as a function of temperature.

FC measurements, shown in Fig. 4. Measurement below the bifurcation shows the downturn occurring at higher temperatures than the Sm as well over a larger temperature range.

Attempts to fit the upper magnetic region to the Curie Weiss law for the Sm variant requires the use of a Van Vleck contribution [35]. The data can be fit as:

$$\chi^{-1} = \frac{T - \Theta_{CW}}{\chi_0 * (T - \Theta_{CW}) + C} \tag{1}$$

Attempting such a fit still results in no linear portion of the inverse susceptibility, excluding the meaningfulness of any extracted constants from the Curie-Weiss analysis. Fitting of the La analog gives C =1.645(1) emu K mol⁻¹ Oe⁻¹, assuming 1 total magnetic ion per formula unit. As transition metal compounds can experience spin transition between low and high spin states as temperature crosses the spin gap energy, one must consider different situations depending on the crystal field splitting [36–38]. If all high spin, C = 3.06 emu K mol⁻¹ Oe⁻¹, low spin (i.e. Co^{3+} is S = 0), C = 0.813 emu K mol^{-1} Oe^{-1} , both out of range of our extracted value. An more likely intermediate spin state $(S_{C_0} = 0, S_{C_r} = 3/2, S_{F_e} = 5/2, S_{M_n} = 1)$ gives C = 1.81 emu K mol⁻¹ Oe⁻¹, close to our value. We see from this that even in complex disordered systems that CW analysis if applied carefully can serve to help understand the likely spin configuration, with further experiments such as X-ray magnetic circular dichroism (XMCD) available to investigate the systems magnetic behavior.

Measurements of magnetization as a function of field in Fig. 5a show no saturation in magnetic moment up to 7 T, with hysteresis emerging and closing between the two magnetic transitions. This ferromagnetic behavior is likely to arise from spin canting in the transition metal sublattice, as discussed further below. Further the hysteresis is often not centered around the origin, and changes position with temperature. The exchange bias and coercive field are defined as:

$$H_{EB} = \frac{H_1 + H_2}{2} \tag{2}$$

Plotting this as a function of temperature is shown in Fig. 5b. Two items of interest are seen in this plot. One, the coercive field does not decrease with increasing temperature but instead goes through two peaks near the magnetic transitions. Second, this behavior is also supported by the variation in exchange bias, indicating interactions

Table 3 Summary of magnetic behavior of parent compounds of HEO SmMO3, where T_N , T_{SR2} , T_{SR1} , T_{SSW} , and T_{Comp} are the Neel temperature, spin reorientation temperatures 1 and 2, spin switching transition, and compensation temperature respectively.

	T_N	T_{SR2}	T_{SR1}	T_{SSW}	T_{Comp}
SmCoO ₃ [45]	_	-	-	-	-
SmCrO ₃ [46]	191 K	34 K	-	-	-
SmFeO ₃ [15]	680 K	480 K	450 K	278.5 K	3.9 K
$SmMnO_3$ [47]	60 K	-	-	_	9 K

between the two magnetic sublattices at different energy scales. The ability to have a tunable exchange bias with varying disorder and temperature is highly desired for spintronic applications and has been demonstrated for systems exhibiting antiferromagnetic and spin glass coupling [39,40]. Current research has explored this in other high entropy perovskites due to the high degree of disorder, with such systems also investigated for their magnetocaloric behavior [41–43]. The temperature dependent magnetic entropy change was calculated based on interpolated MvH behavior. Figure S2 shows transitions at a wide range of temperatures, but no peak surpasses or matches the magnitude of commonly chosen magnetocaloric candidates [44].

To better understand the nature of this system's magnetic behavior, it is best put in context of the parent compounds it is derived from. Such behavior is summarized in Table 3. SmFeO₃ for example, orders antiferromagnetically below T = 680 K, with weak ferrimagnetism present from the canted spins of the Fe sublattice [15]. As the system is cooled further, a spin switching transition occurs, whereupon it later reaches a compensation temperature by the increased magnitude of the FM Sm moment opposite of the Fe moment. Similarly, for SmCrO₃ and SmMnO₃, there exists a canted antiferromagnetic ordering along with a spin reorientation of the Cr lattice and a compensation temperature of the Mn and Sm moments, while SmCoO₃ exhibits paramagnetic behavior [45-52]. From these we can see that the first broad transition in HEO SmMO₃ is likely the AFM ordering of the TM sublattice, with the second broad transition involving the orientation of the Sm sublattice, supported by the weaker magnetic behavior for the La analog at low temperature. We see that the "high entropy" effect has altered the transition temperatures for this material compared to the parent as well as removed this large reversal in magnetization seen for Fe, Mn, Cr.

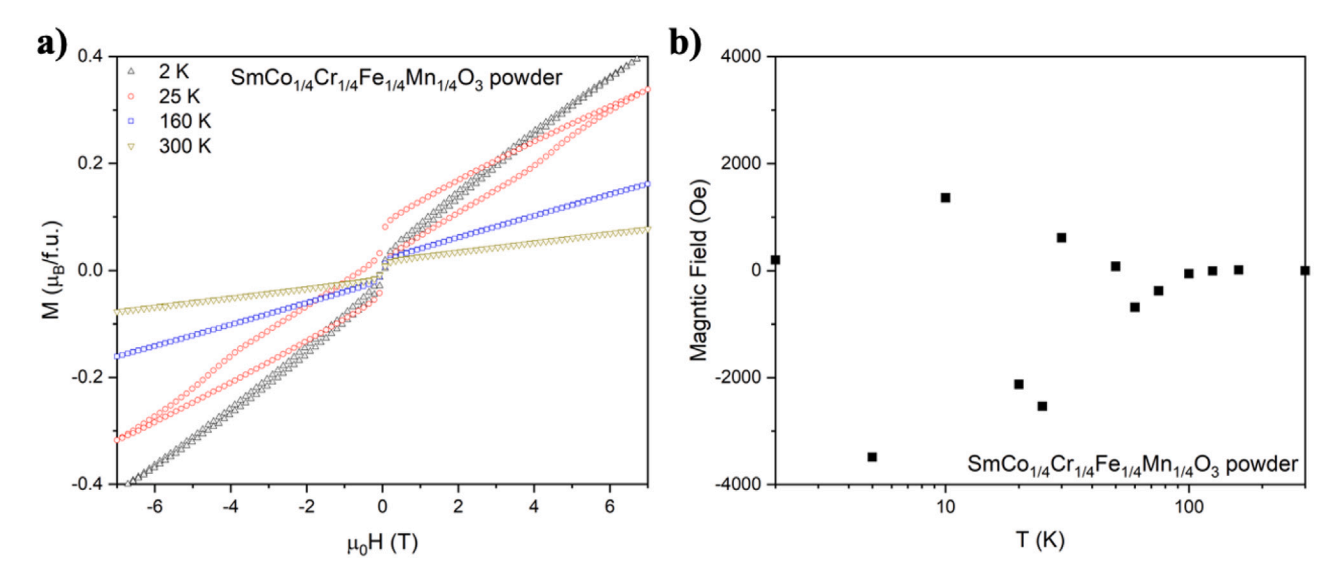
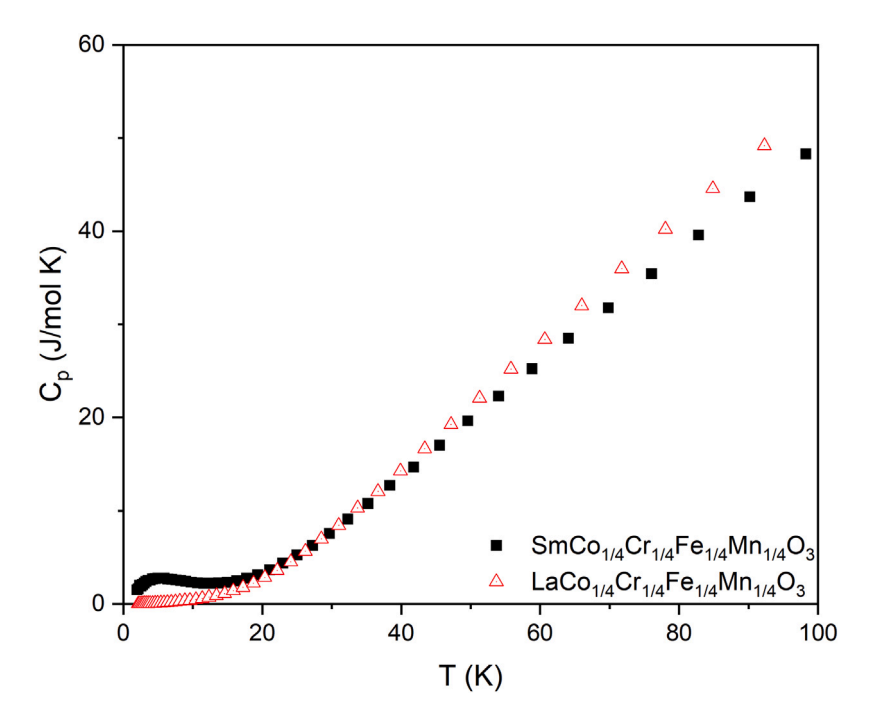


Fig. 5. (a) Magnetization as a function of field for $SmCo_{1/4}Cr_{1/4}Fe_{1/4}Mn_{1/4}O_3$ powder over multiple temperatures. (b) A plot of the exchange bias $(H_{EB} = [H_1 + H_2]/2)$ for $SmCo_{1/4}Cr_{1/4}Fe_{1/4}Mn_{1/4}O_3$ powder over multiple temperatures.



 $\textbf{Fig. 6.} \ \ \text{Heat capacity as a function of temperature for single crystal } \ \ \text{SmCo}_{1/4} \text{Cr}_{1/4} \text{Fe}_{1/4} \text{Mn}_{1/4} \text{O}_3 \ \ \text{and } \ \ \text{LaCo}_{1/4} \text{Cr}_{1/4} \text{Fe}_{1/4} \text{Mn}_{1/4} \text{O}_3 \ \ \text{powder.}$

3.4. Heat capacity

Heat capacity data, specifically C_p/T , give no sign of magnetic ordering in the presence of sharp anomalies. A broad hump is seen in C_p as a function of temperature for Fig. 6, plotted below $T=100~\mathrm{K}$ to highlight the magnetic features. This hump occurs below both ordering transitions seen in magnetic susceptibility and could be a Schottky contribution. Comparison between the La analog shows C_{mag} being most evident below T~20 K. After appropriate scaling is applied, subtraction of the C_{lat} can be done using the La analog, upon which magnetic entropy can be obtained, extrapolating down to $T=0~\mathrm{K}$ with the assumption C_p/T approaches 0. The entropy saturates at approximately 7.5 J/mol K, exceeding Rln(2) by 30% as shown in Fig. 7a. Point charge calculation performing using PyCrystalField shown in Fig. 7b gives an effective S=1/2 ground state. The entropy offset is unexpected but given the potential difference in stoichiometry

between the two analogs, as well as difference in local environment and contributions of the transition metal spins. More work should be pursued to understand proper use of effective analogs for high entropy systems.

4. Conclusion

Overall, the usefulness of single crystals in the design process of high entropy oxides for magnetic applications is demonstrated. We see the presence of single ion anisotropy in the Sm-containing multicomponent transition metal perovskite with magnetic behavior distinct from its parents. The field dependent behavior is of particular interest due to the variability at different temperature regimes for magnetocaloric behavior and tunable exchange bias. Nonmagnetic analogs are utilized to get a better understanding of the compared behavior, in heat capacity measurements specifically. Further directions should utilize this

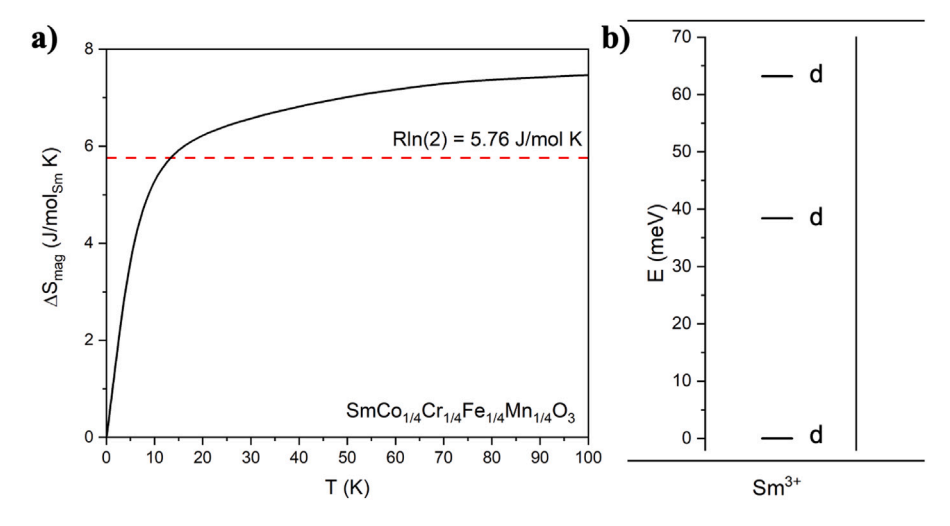


Fig. 7. (a) The magnetic entropy for $SmCo_{1/4}Cr_{1/4}Fe_{1/4}Mn_{1/4}O_3$ obtained by integrated C_{mag}/T data after subtracting the scaled La analog. (b) The computed single ion crystal field for Sm^{3+} in the perovskite structure. Doublet states are indicated by d.

development in single crystal growth to undergo further measurements such as single crystal pair distribution function to understand the development of short-range order. XMCD can be used to get transition element resolved information on the magnetic transitions and spin canting, with electron microscopy characterization to look for atomic scale homogeneity.

CRediT authorship contribution statement

Lucas A. Pressley: Conceptualization, Methodology, Software, Validation, Formal analysis, Investigation, Writing – original draft, Writing – review & editing, Visualization. Hector K. Vivanco: Methodology, Investigation, Formal analysis, Data curation, Writing – review & editing, Visualization. Tanya Berry: Methodology, Investigation, Formal analysis, Writing – review & editing, Visualization. Maxime A. Siegler: Investigation, Formal analysis, Data curation, Writing – review & editing, Visualization, Resources. Tyrel M. McQueen: Conceptualization, Methodology, Software, Data curation, Writing – review & editing, Resources, Supervision, Project administration, Funding acquisition.

Declaration of competing interest

The authors declare that they have no known competing financial interests or personal relationships that could have appeared to influence the work reported in this paper.

Data availability

Raw data from the facility will be available at https://data.paradim. org/. Code used for magnetic entropy calculations is available at https://materialsautomated.github.io/.

Acknowledgments

This work was funded by the Platform for the Accelerated Realization, Analysis, and Discovery of Interface Materials (PARADIM), a National Science Foundation Materials Innovation Platform (NSF DMR-2039380). The MPMS was funded by the National Science Foundation, USA, Division of Materials Research, Major Research Instrumentation Program, under Award 1828490.

Appendix A. Supplementary data

Supplementary material related to this article can be found online at https://doi.org/10.1016/j.jcrysgro.2023.127262.

References

- B. Cantor, I.T.H. Chang, P. Knight, A.J.B. Vincent, Microstructural development in equiatomic multicomponent alloys, Mater. Sci. Eng. A 375–377 (2004) 213–218, http://dx.doi.org/10.1016/j.msea.2003.10.257.
- [2] J.-W. Yeh, S.-K. Chen, S.-J. Lin, J.-Y. Gan, T.-S. Chin, T.-T. Shun, C.-H. Tsau, S.-Y. Chang, Nanostructured high-entropy alloys with multiple principle elements: Novel alloy design concepts and outcomes, Adv. Eng. Mater. 6 (5) (2004) 299–303, http://dx.doi.org/10.1002/adem.200300567.
- [3] M.C. Gao, J.-W. Yeh, P.K. Liaw, Z. Yong, High-Entropy Alloys: Fundamentals and Applications, first ed., Springer International Publishing, Cham, 2016.
- [4] B.L. Musicó, D. Gilber, T.Z. Ward, K. Page, E. George, J. Yan, D. Mandrus, V. Keppens, The emergent field of high entropy oxides: Design, prospects, challenges, and opportunities for tailoring material properties, APL Mater. 8 (4) (2020) http://dx.doi.org/10.1063/5.0003149.
- [5] B. Jiang, C.A. Bridges, R.R. Unocic, K.P. Chaitanya, V.R. Cooper, Y. Zhang, D.-Y. Lin, K. Page, Probing the local site disorder and distortion in pyrochlore high-entropy oxides, J. Am. Chem. Soc. 143 (11) (2021) 4193–4204, http://dx.doi.org/10.1021/jacs.0c10739.
- [6] J. Dabrowa, M. Stygar, A. Mikuła, A. Knapik, K. Mroczka, W. Tejchman, M. Danielewski, M. Martin, Synthesis and microstructure of the (Co,Cr,Fe,Mn,Ni)₃O₄ high entropy oxide characterized by spinel structure, Mater. Lett. 216 (2018) 32–26, http://dx.doi.org/10.1016/j.matlet.2017.12.148.
- [7] A. Sarkar, R. Kruk, H. Hahn, Magnetic properties of high entropy oxides, Dalton Trans. 50 (6) (2021) 1973–1982, http://dx.doi.org/10.1039/d0dt04154h.
- [8] G.H.J. Johnstone, M.U. González-Rivas, K.M. Taddei, R. Sutarto, G.A. Sawatzky, R.J. Green, M. Oudah, A.M. Hallas, Entropy engineering and tunable magnetic order in the spinel high-entropy oxide, J. Am. Chem. Soc. 144 (45) (2022) 20590–20600, http://dx.doi.org/10.1021/jacs.2c06768.
- [9] V.M. Goldschmidt, Die Gesetze der Krystallochemie, Naturwissenschaften 14 (1926) 477–485, http://dx.doi.org/10.1007/BF01507527.
- [10] C. Kinsler-Fedon, Q. Zheng, Q. Huang, E.S. Choi, J. Yan, H. Zhou, D. Mandrus, V. Keppens, Synthesis, characterization, and single-crystal growth of a highentropy rare-earth pyrochlore oxide, Phys. Rev. Mater. 4 (10) (2020) 104411, http://dx.doi.org/10.1103/PhysRevMaterials.4.104411.
- [11] B.C. Sales, K. Jin, H. Bei, J. Nichols, M.F. Chisholm, A.F. May, N.P. Butch, A.D. Christianson, M.A. McGuire, Quantum critical behavior in the asymptotic limit of high disorder in the medium entropy alloy NiCoCr_{0.8}, Npj Quantum Mater. 2 (1) (2017) 33.
- [12] M. Pianassola, M. Loveday, B.C. Chakoumakos, M. Koschan, C.L. Melcher, M. Zhuravleva, Crystal growth and elemental homogeneity of the multicomponent rare-earth garnet $(Lu_{1/6}Y_{1/6}Ho_{1/6}Dy_{1/6}Tb_{1/6}Gd_{1/6})_3Al_5O_{12}$, Cryst. Growth Des. 20 (10) (2020) 6769–6776, http://dx.doi.org/10.1021/acs.cgd.0c00887.
- [13] M. Feuerbacher, E. Würtz, A. Kovács, C. Thomas, Single-crystal growth of a FeCoCrMnAl high-entropy alloy, Mater. Res. Lett. 5 (2) (2017) 128–134, http://dx.doi.org/10.1080/21663831.2016.1234516.
- [14] M. Pianassola, B.C. Chakoumakos, C.L. Melcher, M. Zhuravleva, Crystal growth and phase formation of high-entropy rare-earth aluminum perovskites, Cryst. Growth Des. 23 (1) (2023) 480–488, http://dx.doi.org/10.1021/acs.cgd.2c01130.
- [15] S. Cao, H. Zhao, B. Kang, J. Zhang, W. Ren, Temperature induced spin switching in SmFeO₃ single crystal, Sci. Rep. 4 (5960) (2014) http://dx.doi.org/10.1038/ srep05960.

- [16] J.A. Hofmann, A. Paskin, K.J. Tauer, R.J. Weiss, Analysis of ferromagnetic and antiferromagnetic second-order transitions, J. Phys. Chem. Solids 1 (1–2) (1956) 45–60, http://dx.doi.org/10.1016/0022-3697(56)90010-5.
- [17] A. Tari, The Specific Heat of Matter At Low Temperatures, Imperial College Press, 2003
- [18] G.M. Sheldrick, SHELXT-Integrated space-group and crystal-structure determination, Acta Crystallogr. A 71 (2015) 3–8, http://dx.doi.org/10.1107/ S2053273314026370.
- [19] K. Momma, F. Izumi, VESTA: a three-dimensional visualization system for electronic and structural analysis, J. Appl. Crystallogr. 41 (2008) 654–658, http://dx.doi.org/10.1107/S0021889808012016.
- [20] J.D. Bocarsly, R.F. Need, R. Seshadri, S.D. Wilson, Magnetoentropic signatures of skyrmionic phase behavior in FeGe, Phys. Rev. B 97 (2018) 100404, http: //dx.doi.org/10.1103/PhysRevB.97.100404.
- [21] A. Scheie, PyCrystalField: software for calculation, analysis and fitting of crystal electric field Hamiltonians, J. Appl. Crystallogr. 54 (2021) 356–362, http://dx. doi.org/10.1107/S160057672001554X.
- [22] A. Navrotsky, O.J. Kleppa, Thermodynamics of formation of simple spinels, J. Inorg. Nucl. Chem. 30 (2) (1968) 479–498, http://dx.doi.org/10.1016/0022-1902(68)80475-0.
- [23] N. Alexandra, Thermodynamics of formation of some compounds with the Pseudobrookite structure and of the $FeTi_2O_5$ - Ti_3O_5 solid solution series, Am. Mineral. 60 (3–4) (1975) 249–256.
- [24] C.M. Rost, E. Sachet, T. Borman, A. Moballegh, E.C. Dickey, D. Hou, J.L. Jones, S. Curtarolo, J.-P. Maria, Entropy-stabilized oxides, Nature Commun. 6 (8485) (2015) http://dx.doi.org/10.1038/ncomms9485.
- [25] R.J. Spurling, E.A. Lass, X. Wang, K. Page, Entropy-driven phase transitions in complex ceramic oxides, Phys. Rev. Mater. 6 (2022) 090301, http://dx.doi.org/ 10.1103/PhysRevMaterials.6.090301.
- [26] R. Witte, A. Sarkar, R. Kruk, B. Eggert, R.A. Brand, H. Wende, H. Hahn, High-entropy oxides: An emerging prospect for magnetic rare-earth transition metal perovskites, Phys. Rev. Mater. 3 (3) (2019) 034406, http://dx.doi.org/10.1103/PhysRevMaterials.3.034406.
- [27] J. Zhang, H. Zheng, Y. Ren, J. Mitchell, High-pressure floating-zone growth of perovskite nickelate LaNiO₃ single crystals, Cryst. Growth Des. 17 (5) (2017) 2730–2735, http://dx.doi.org/10.1021/acs.cgd.7b00205.
- [28] H. Zheng, J. Zhang, B. Wang, D. Phelan, M.J. Krogstad, Y. Ren, W.A. Phelan, O. Chmaissem, B. Poudel, J.F. Mitchell, High p_{O2} floating zone crystal growth of the perovskite nickelate PrNiO₃, Crystals 9 (7) (2019) 324, http://dx.doi.org/10.3390/cryst9070324.
- [29] I.D. Brown, Recent developments in the methods and applications of the bond valence model, Chem. Rev. 109 (12) (2009) 6858–6919, http://dx.doi.org/10. 1021/cr900053k.
- [30] J.M. Schneider, How high is the entropy in high entropy ceramics? J. Appl. Phys. 130 (150903) (2021) http://dx.doi.org/10.1063/5.0062523.
- [31] M. Brahlek, M. Gazda, V. Keppens, A.R. Mazza, S.J. McCormack, A. Mielewczyk-Gryń, B. Musico, K. Page, C.M. Rost, S.B. Sinnott, C. Toher, T.Z. Ward, A. Yamamoto, What is in a name: Defining "high entropy" oxides, APL Materials 10 (11) (2022) 110902, http://dx.doi.org/10.1063/5.0122727.
- [32] O.F. Dippo, K.S. Vecchio, A universal configurational entropy metric for high-entropy materials, Scr. Mater. 201 (113974) (2021) http://dx.doi.org/10.1016/j.scriptamat.2021.113974.
- [33] S. Geller, Crystal structure of gadolinium orthoferrite, GdFeO₃, J. Chem. Phys. 24 (6) (1956) 1236–1239.
- [34] A.M. Glazer, The classification of tilted octahedra in perovskites, Acta Crystallogr. B B28 (1972) 3384–3392, http://dx.doi.org/10.1107/S0567740872007976.
- [35] Y. Takikawa, S. Ebisu, N. Shoichi, Van vleck paramagnetism of the trivalent Eu ions, J. Phys. Chem. Solids 71 (11) (2010) 1592–1598, http://dx.doi.org/10. 1016/j.jpcs.2010.08.006.

- [36] S.G. Ovchinnikov, Y.S. Orlov, I.A. Nekrasov, Z.V. Pchelkina, Electronic structure, magnetic properties, and mechanism of the insulator metal transition in LaCoO₃ taking into account strong electron correlations, J. Exp. Theor. Phys. 112 (2011) 140–151, http://dx.doi.org/10.1134/S1063776110061159.
- [37] Y. Tanabe, S. Sugano, On the absorption spectra of complex ions II, J. Phys. Soc. Japan 9 (5) (1954) 753–766, http://dx.doi.org/10.1143/JPSJ.9.753.
- [38] J.B. Goodenough, P.M. Raccah, Complex vs band formation in perovskite oxides, J. Appl. Phys. 36 (1031) (1965) http://dx.doi.org/10.1063/1.1714087.
- [39] E. Maniv, R.A. Murphy, S.C. Haley, S. Doyle, C. John, A. Maniv, S.K. Ramakrishna, Y.-L. Tang, P. Ercius, R. Ramesh, A.P. Reyes, J.R. Long, J.G. Analytis, Exchange bias due to coupling between coexisting antiferromagnetic and spinglass orders, Nat. Phys. 17 (2021) 525–530, http://dx.doi.org/10.1038/s41567-020-01123-w.
- [40] M. Ali, P. Adie, C.H. Marrows, D. Greig, B.J. Hickey, R.L. Stamps, Exchange bias using a spin glass, Nature Mater. 6 (2007) 70–75, http://dx.doi.org/10. 1038/nmat1809.
- [41] P.B. Meisenheimer, J.T. Heron, Oxides and the high entropy regime: new mix for engineering physical properties, MRS Adv. 5 (2020) 3419–3436, http://dx.doi.org/10.1557/adv.2020.295.
- [42] A.R. Mazza, E. Skoropata, Y. Sharma, J. Lapano, T.W. Heitmann, B.L. Musico, V. Keppens, Z. Gai, J.W. Freeland, T.R. Charlton, M. Brahlek, A. Moreo, E. Dagotto, T.Z. Ward, Designing magnetism in high entropy oxides, Adv. Sci. 9 (10) (2022) 2200391, http://dx.doi.org/10.1002/advs.202200391.
- [43] Y. Yin, F. Shi, G.-Q. Liu, X. Tan, J. Jiang, A. Tiwari, B. Li, Spin-glass behavior and magnetocaloric properties of high-entropy perovskite oxide, Appl. Phys. Lett. 120 (8) (2022) http://dx.doi.org/10.1063/5.0081688.
- [44] D. Liu, M. Yue, J. Zhang, T.M. McQueen, J.W. Lynn, X. Wang, Y. Chen, J. Li, R.J. Cava, X. Liu, Z. Altounian, Q. Huang, Origin and tuning of the magnetocaloric effect in the magnetic refrigerant Mn_{1.1}Fe_{0.9}(P_{0.8}Ge_{0.2}), Phys. Rev. B 79 (2009) 014435, http://dx.doi.org/10.1103/PhysRevB.79.014435.
- [45] V.A. Dudnikov, Y.S. Orlov, L.A. Solovyov, S.N. Vereshchagin, S.Y. Gavrilkin, A.Y. Tsvetkov, D.A. Velikanov, M.V. Gorev, S.V. Novikov, S.G. Ovchinnikov, Effect of multiplicity fluctuation in Cobalt ions on crystal structure, magnetic and electrical properties of NdCoO₃ and SmCoO₃, Molecules 25 (6) (2020) 1301, http://dx.doi.org/10.3390/molecules25061301.
- [46] M. Tripathi, R.J. Choudhary, D.M. Phase, T. Chatterji, H.E. Fischer, Evolution of magnetic phases in SmCrO₃: A neutron diffraction and magnetomatric study, Phys. Rev. B 96 (17) (2017) 174421, http://dx.doi.org/10.1103/PhysRevB.96. 174421
- [47] J.-G. Cheng, J.-S. Zhou, J.B. Goodenough, Y.T. Su, Y. Sui, Y. Ren, Exchange field on the rare earth Sm³⁺ in a single crystal perovskite SmMnO₃, Phys. Rev. B 84 (10) (2011) 104415, http://dx.doi.org/10.1103/PhysRevB.84.104415.
- [48] Y.K. Jeong, J.-H. Lee, S.-J. Ahn, H.M. Jang, Temperature-induced magnetization reversal and ultra-fast magnetic switch at low field in SmFeO₃, Solid State Commun. 152 (13) (2012) 1112–1115.
- [49] A. Panchwanee, V.R. Reddy, A. Gupta, Mössbauer and magnetization study of polycrystalline multiferroic SmFeO₃, J. Magn. Magn. Mater. 448 (2018) 38–42, http://dx.doi.org/10.1016/j.jmmm.2017.04.054.
- [50] G. Oliveira, R. Teixeira, R. Moreira, J. Correia, J. Araújo, A. Lopes, Local inhomogeneous state in multiferroic SmCrO₃, Sci. Rep. 10 (1) (2020) 1–12.
- [51] J.-S. Jung, A. Iyama, H. Nakamura, M. Mizumaki, N. Kawamura, Y. Wakabayashi, T. Kimura, Magnetocapacitive effects in the Néel N-type ferrimagnet SmMnO₃, Phys. Rev. B 82 (21) (2010) 212403.
- [52] N. Ivanova, N. Kazak, C. Michel, A. Balaev, S. Ovchinnikov, Low-temperature magnetic behavior of the rare-earth cobaltites GdCoO₃ and SmCoO₃, Phys. Solid State 49 (2007) 2126–2131.